Linear frequency modulation photoacoustic radar: Optimal bandwidth and signal-to-noise ratio for frequency-domain imaging of turbid media

Bahman Lashkari and Andreas Mandelis[a)]
Center for Advanced Diffusion-Wave Technologies (CADIFT), Department of Mechanical and Industrial Engineering, University of Toronto, Toronto, M5S 3G8, Canada

(Received 7 March 2011; revised 19 May 2011; accepted 19 May 2011)

The development of the pulse compression photoacoustic (PA) radar using linear frequency modulation (LFM) demonstrated experimentally that spectral matching of the signal to the ultrasonic transducer bandwidth does not necessarily produce the best PA signal-to-noise ratio, and it was shown that the optical and acoustic properties of the absorber will modify the optimal bandwidth. The effects of these factors are investigated in frequency-domain (FD) PA imaging by employing one-dimensional and axisymmetric models of the PA effect, and a Krimholtz–Leedom–Matthaei model for the employed transducers. LFM chirps with various bandwidths were utilized and transducer sensitivity was measured to ensure the accuracy of the model. The theory was compared with experimental results and it was shown that the PA effect can act as a low-pass filter in the signal generation. Furthermore, with the PA radar, the low-frequency behavior of two-dimensional wave generation can appear as a false peak in the cross correlation signal trace. These effects are important in optimizing controllable features of the FD-PA method to improve image quality.
© *2011 Acoustical Society of America*. [DOI: 10.1121/1.3605290]

PACS number(s): 43.35.Ud, 43.35.Sx [CCC] Pages: 1313–1324

I. INTRODUCTION

Photothermoacoustics or photoacoustics (PA) is the generation of acoustic waves as a result of light energy absorption and subsequent thermo-elastic expansion in a material. This effect provides a promising technology for non-invasive medical imaging. In the past decade, a variety of biomedical applications has been investigated with this imaging technique, with major focus on breast cancer.[1] PA imaging can be classified according to the employed irradiation source, either using powerful nanosecond laser pulses or low power intensity-modulated continuous wave (CW) laser irradiation. To-date pulsed laser PA has captured almost exclusive attention due to the stronger induced signal and straightforward signal processing algorithms.

The application of CW signals has a long history in radar technology in the quest for increasing operating range while employing limited transmission power. Pulse compression by matched filtering could solve this problem.[2] Matched filtering enables the detection of a pre-known signal immersed in Gaussian white noise,[3] therefore a long duration coded waveform with moderate power could replace short high-power pulses. The matched filter for this coded waveform was shown to be the complex conjugate of the transmitted signal.[4,5] Pulse compression can increase the signal-to-noise ratio (SNR) without deteriorating the range resolution, where its effectiveness depends on the time-bandwidth product of the transmitted waveform. Despite the unlimited variety of the input waveforms, they can all be classified according to the time-bandwidth product.[6] Applying judicious windowing to the receiver, in view of the trade-off between SNR degradation and sidelobe level has been discussed extensively in the literature.[7,8] These findings formed the foundation for employing the CW technique in the field of ultrasound and, later on, our introduction of the PA radar.

Although the use of coded waveforms in ultrasound is more recent than radar technology, nevertheless the smaller feasible time-bandwidth product in ultrasound is a major obstacle in the implementation of the CW ultrasonic radar.[9,10] O'Donnell[11] considered the possible time-bandwidth product and safety limitations on maximum transmission acoustic intensity in medical ultrasound, and predicted that 15 to 20 dB SNR improvement is possible. The frequency dependent acoustic attenuation was shown to reduce the effective time-bandwidth product.[12] Pollakowski and Ermert[13] pointed out that by using square wave pseudochirps, it is possible to increase the signal amplitude without changing the amplitude of the transmitted power, also while reducing the sidelobe levels. The same research group also determined that the optimal bandwidth of the transducer for a cosine square shaped transfer function is 1.14 times the conventional −6 dB bandwidth of the transducer.[14] It was shown that the transducer can have an effect similar to a frequency weighting window and reduce the sidelobes.[14,15] A clinical comparison between the coded excitation and pulsed ultrasound was carried out by Pedersen *et al.*[16] and revealed that CW ultrasound can significantly increase the imaging depth by almost 2 cm. A comprehensive overview of the application of the modulated excitation in medical ultrasound was presented in a series of papers by Misaridis and Jensen.[17–19]

CW or frequency-domain (FD) PA was first proposed and implemented by our group, featuring heterodyne

[a)]Author to whom correspondence should be addressed. Electronic mail: mandelis@mie.utoronto.ca

Redistribution subject to ASA license or copyright; see http://acousticalsociety.org/content/terms. Download to IP: 128.100.49.199 On: Thu, 24 Mar 2016 21:40:34

modulation and lock-in detection of a frequency swept laser source.[20,21] This work was backed by a detailed theoretical analysis of the frequency-domain photoacoustic transient generation and propagation. The theory was based on one-dimensional thermal-wave and displacement potential equations in a two-layered model (scattering and absorbing layers). The solution was attained by utilizing the Fourier transformation method.[20] The two-layered model facilitated a proper analysis of the back-propagating transients, consistent with the utilized reflection-mode detection. Later on, employing an analog-to-digital convertor, the system became more capable of utilizing different signal processing methods. Matched filter compression and heterodyne mixing were implemented and tested.[22,23] The PA system was evaluated by imaging different turbid-phantoms, *ex vivo* chicken breast specimens and an *in vivo* human finger.[24] The maximum depths of the imaged inclusions were 9 and 17 mm of chicken breast tissue for high- and low-frequency transducers (3.5 MHz and 500 kHz), respectively.[22,23] To be able to perform a comparative study between pulsed PA and FD-PA, a pulsed laser source was added to the system, producing a dual-mode PA imaging system. The two modalities were compared with respect to the maximum detectable depth.[25]

The FD-PA method using single-frequency modulation was later implemented by Maslov and Wang for microscopic imaging a few millimeters below the skin surface. The so-called PAM (photoacoustic microscope) demonstrated a lateral and axial resolution of 600 and 700 μm, respectively. However, the achieved SNR was one order of magnitude lower than that of the pulsed PA image.[26] It is consistent with a very recent theoretical account of both modalities by Petschke and La Riviére.[27]

Implementation of coded excitation in PA was created by utilizing Golay codes. The use of this kind of coding is widely practiced in ultrasound with the major advantage of excluding the sidelobe problem as compared with frequency modulated chirps. A high-power laser diode at a wavelength of 808 nm and pulse repetition frequencies between 20 kHz to 1 MHz was utilized to generate the coded irradiation. The experimental results support the feasibility of this system for small animal imaging.[28]

In our previous work,[29] we showed that the FD method possesses a phase channel, in addition to the amplitude channel. We introduced the inverse of the standard deviation of the phase as a statistical tool, capable of image generation from the phase channel. It was shown that the optimal bandwidth for the modulated waveform is not exclusively defined by the transducer bandwidth, but also by the physical properties of the material (particularly, absorption coefficient and acoustic attenuation). It was argued that there is no need for extra windowing of the received signal, since the transducer acts as a filter that reduces the sidelobes. In this paper, the PA wave generation and propagation is theoretically investigated, and the transducer function is modeled by means of an electrical circuit model. The optimal bandwidth of the modulated waveform is investigated both experimentally and theoretically. The roles of the various parameters—transducer, PA effect, acoustic attenuation, geometry of wave generation, and propagation—are discussed.

II. THEORY OF PHOTOACOUSTIC WAVE GENERATION AND PROPAGATION

To analyze the generation and propagation of the ultrasonic waves induced by laser excitation, the diffusive propagation of laser light in turbid media must be determined and the velocity potential equation must be solved considering the absorber and surrounding media. The PA wave generation and propagation can be investigated employing the Green-function method.[30] Another method that can be used is Fourier analysis.[31] We pursue the latter method, since it uses transfer functions which are more helpful in understanding system behavior in the frequency-domain. Figure 1 shows a two-layer material consisting of a chromophore object (absorbing medium) lying below a layer of scattering medium. As the chromophore absorbs the laser energy, pressure waves are generated and propagate through both media. We do not consider the effect of heat conduction and viscosity dissipation; these effects were shown to be minor in photoacoustics.[31] Also, transverse wave generation is neglected due to its large acoustic attenuation in tissue.[32] A one-dimensional (1D) as well as a two-dimensional (2D) axially symmetrical formulation are presented here. By comparing these models with experimental results, the range of applicability of each model can be assessed.

A. One-dimensional PA wave generation

Using the Fourier method, a 1D PA wave generation and propagation analysis is presented which follows earlier approaches by Mandelis *et al*.[33] and Fan *et al*.[21]

In the 1D model, the optical excitation reaching the absorbing medium can be estimated by the exponential attenuation

$$\tilde{I}(f) = \mathcal{F}\left[I_0(t)e^{-\mu_{\mathrm{eff}}L}\right] = \tilde{I}_0(f)e^{-\mu_{\mathrm{eff}}L}, \qquad (1)$$

where I_0 is the laser intensity on the surface and I is the intensity reaching the absorber, μ_{eff} is the effective optical attenuation coefficient of tissue, L is the thickness of the scattering medium, and $\mathcal{F}$ and tilde symbolize the Fourier transformation operation. In the Fourier domain, the velocity potentials in the absorbing (a) and scattering (s) medium, respectively, are governed by

$$\nabla^2\tilde{\phi}_a(\boldsymbol{r}, f) + k_a^2\tilde{\phi}_a(\boldsymbol{r}, f) = \frac{\beta_a\mu_a}{\rho_a C_p}\tilde{I}(\boldsymbol{r}, f)e^{-\mu_a z}, \qquad (2a)$$

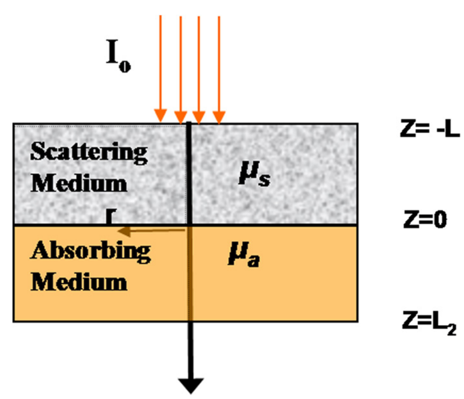

FIG. 1. (Color online) Simple model of photoacoustic signal generation.

Redistribution subject to ASA license or copyright; see http://acousticalsociety.org/content/terms. Download to IP: 128.100.49.199 On: Thu, 24 Mar 2016 21:40:34

$$\nabla^2 \tilde{\phi}_s(\boldsymbol{r}, f) + k_s^2 \tilde{\phi}_s(\boldsymbol{r}, f) = 0, \tag{2b}$$

where $k_a = \omega / c_a$ and $k_s = \omega / c_s$ are absorbing and scattering medium wavenumbers, respectively; c_a and c_s is the speed of sound in the absorbing and scattering medium, respectively; ω is the angular frequency, $\omega = 2\pi f$; $\boldsymbol{r}$ is a position vector; $\tilde{\phi}_a$and$\tilde{\phi}_s$ are Fourier transforms of velocity potentials in the absorbing and scattering medium, respectively; μ_a is the absorption coefficient of the absorbing medium (e.g., a cancerous lesion); $\rho_a$andρ_s are the density of the absorbing and scattering media, respectively; β_a is the thermal expansion coefficient; and C_p is the specific heat capacity.

This problem can be solved readily in the one dimensional (z axis) case

$$\tilde{\phi}_a(z,f) = \left(C_1 e^{-jk_a z} + C_2 e^{+jk_a z} + C_s e^{-\mu_a z}\right)\tilde{I}(f); \quad z \geq 0, \tag{3a}$$

$$\tilde{\phi}_s(z,f) = \left(C_3 e^{-jk_s z} + C_4 e^{+jk_s z}\right)\tilde{I}(f); \quad -L \leq z \leq 0. \tag{3b}$$

Applying the radiation boundary condition (BC) for outward moving waves only, we set $C_2 = C_3 = 0$. In addition, there should be pressure and velocity continuity at the interface

$$\begin{aligned}\tilde{p}_s(z=0, f) = \tilde{p}_a(z=0, f) \Rightarrow \rho_s\, j\omega \tilde{\phi}_s(0, f) \\ = \rho_a\, j\omega \tilde{\phi}_a(0, f)\end{aligned} \tag{4a}$$

and

$$\left.\frac{d\tilde{\phi}_s(z,f)}{dz}\right|_{z=0} = \left.\frac{d\tilde{\phi}_a(z,f)}{dz}\right|_{z=0}, \tag{4b}$$

which yield

$$C_S = \frac{\Gamma_a}{\rho_a c_a^2} \frac{\mu_a}{(\mu_a^2 + k_a^2)}, \tag{5a}$$

$$C_1 = \frac{\frac{-1}{\rho_s c_s} + \frac{j\mu_a}{\omega \rho_a}}{\left(\frac{1}{\rho_a c_a} + \frac{1}{\rho_s c_s}\right)} C_S, \tag{5b}$$

$$C_4 = \frac{j\mu_a + k_a}{\rho_s \omega \left(\frac{1}{\rho_a c_a} + \frac{1}{\rho_s c_s}\right)} C_S. \tag{5c}$$

In Equation (5a), $\Gamma_a = \beta_a c_a^2 / C_p$ is the efficiency of thermoacoustic excitation often called the Grüneisen coefficient. The pressure detected by the transducer, assuming that it is located at $z = -L$, can thus be determined:

$$\tilde{p}_s(-L,f) = -\rho_s j\omega \tilde{\phi}_s(-L,f) = -\rho_s j\omega C_4 e^{-jk_s L} \tilde{I}(f). \tag{6}$$

Finally, from Eqs. (5c) and (6):

$$\tilde{p}_s(-L,f) = \frac{\Gamma_a e^{-\mu_{\text{eff}} L}}{\left(1 + \frac{\rho_a c_a}{\rho_s c_s}\right)} \frac{\mu_a}{\mu_a c_a + j\omega} e^{-jk_s L} \tilde{I}_0(f). \tag{7}$$

This formula is useful in estimating the pressure wave generated under both pulsed and FD-PA excitation.

B. Axially symmetric PA transient generation

While the 1D solution is adequate to analyze numerous applications, especially for high-frequency FD-PA, some effects such as the bipolar shape of a pulsed transient cannot be explained by the 1D model.[30] An axially symmetric formulation and analysis of PA wave generation and propagation is consistent with a symmetric Gaussian laser beam. Our strategy is to simplify the geometry and analyze the temporal evolution of the signal. In the 1D model, the diffusion of laser light in a turbid medium was modeled with an exponential attenuation. The diffusion of light in a scattering medium for axisymmetric model can be calculated either by Monte Carlo analysis or using the diffuse-photon-density wave (DPDW) approximation. An axisymmetric solution of the DPDW is derived based on the Mandelis and Feng[34] formulation and shows that the reduction of the peak fluence has a very good convergence to a spherical scattering source which is spatially heavily damped according to

$$\tilde{I}(f) \approx \frac{1}{2} W_0 \tilde{I}_0(f) \left(\frac{e^{-\mu_{\text{eff}} L}}{L}\right), \tag{8}$$

especially at deep locations.[35] Here W_0 is the beam spot size on the surface. This approximate result or the analytical laser fluence can be used as the source term in the velocity potential equation to solve for the propagation of the pressure transient.

The cylindrical Fourier-domain equations for the velocity potential in the scattering (s) and absorbing (a) media, where the energy source only affects the absorbing medium, are

$$\frac{\partial^2 \tilde{\phi}_a}{\partial z^2} + \frac{1}{r}\frac{\partial}{\partial r}\left(r \frac{\partial \tilde{\phi}_a}{\partial r}\right) + k_a^2 \tilde{\phi}_a = \frac{\beta_a \mu_a}{\rho_a C_p} \tilde{I}(f, r) e^{-\mu_a z}, \tag{9a}$$

$$\frac{\partial^2 \tilde{\phi}_s}{\partial z^2} + \frac{1}{r}\frac{\partial}{\partial r}\left(r \frac{\partial \tilde{\phi}_s}{\partial r}\right) + k_s^2 \tilde{\phi}_s = 0. \tag{9b}$$

Using the Hankel transformation, yields

$$\frac{\partial^2 \hat{\tilde{\phi}}_a}{\partial z^2} - \lambda^2 \hat{\tilde{\phi}}_a + k_a^2 \hat{\tilde{\phi}}_a = \frac{\beta_a \mu_a}{\rho_a C_p} \hat{\tilde{I}}(f, \lambda) e^{-\mu_a z}, \tag{10a}$$

$$\frac{\partial^2 \hat{\tilde{\phi}}_s}{\partial z^2} - \lambda^2 \hat{\tilde{\phi}}_s + k_s^2 \hat{\tilde{\phi}}_s = 0, \tag{10b}$$

where the hat symbolizes the Hankel transform parameter and λ is the Hankel transformation parameter. If we assume $k_s < k_a$, then, for three ranges of λ, the system of equations can be solved. This method is adopted to avoid any indeterminate situations.

Range I: $\lambda < k_s < k_a$. The solutions are

$$\hat{\tilde{\phi}}_a(z,\lambda,f) = C_1 e^{-j\sqrt{k_a^2 - \lambda^2} z} + C_2 e^{\, j\sqrt{k_a^2 - \lambda^2} z} + C_s \hat{\tilde{I}}(f,\lambda) e^{-\mu_a z}, \tag{11a}$$

$$\hat{\tilde{\phi}}_s(z, \lambda, f) = C_3 e^{-j\sqrt{k_s^2 - \lambda^2} z} + C_4 e^{j\sqrt{k_s^2 - \lambda^2} z}. \tag{11b}$$

The coefficient of the particular solution is

Redistribution subject to ASA license or copyright; see http://acousticalsociety.org/content/terms. Download to IP: 128.100.49.199 On: Thu, 24 Mar 2016 21:40:34

$$C_s = \left(\frac{1}{\mu_a^2 + k_a^2 - \lambda^2}\right)\frac{\beta_a \mu_a}{\rho_a C_p}. \quad (12)$$

From the radiation BC, $C_2 = C_3 = 0$.

The other BCs concern the continuity of pressure and velocity at the interface, $z = 0$. They yield

$$C_4 = \frac{\left(\sqrt{k_a^2 - \lambda^2} + j\mu_a\right)}{\left(\sqrt{k_s^2 - \lambda^2} + \frac{\rho_s}{\rho_a}\sqrt{k_a^2 - \lambda^2}\right)}\hat{\tilde{I}}(f,\lambda)C_s, \quad (13)$$

therefore

$$\hat{\tilde{\phi}}_s(z,\lambda,f) = C_4 e^{j\sqrt{k_s^2-\lambda^2}z} = \frac{1}{\sqrt{k_s^2 - \lambda^2} + \frac{\rho_s}{\rho_a}\sqrt{k_a^2 - \lambda^2}}\left(\frac{j}{\mu_a + j\sqrt{k_a^2 - \lambda^2}}\right)\frac{\beta_a\mu_a}{\rho_a C_p} e^{j\sqrt{k_s^2-\lambda^2}z}\hat{\tilde{I}}(f,\lambda). \quad (14)$$

Range II: $k_s < \lambda < k_a$. The solutions are

$$\hat{\tilde{\phi}}_a(z,\lambda,f) = C_1' e^{-j\sqrt{k_a^2-\lambda^2}z} + C_2' e^{j\sqrt{k_a^2-\lambda^2}z} + C_s\hat{\tilde{I}}(f,\lambda)e^{-\mu_a z}, \quad (15a)$$

$$\hat{\tilde{\phi}}_s(z,\lambda,f) = C_3' e^{-\sqrt{\lambda^2-k_s^2}z} + C_4' e^{\sqrt{\lambda^2-k_s^2}z}. \quad (15b)$$

The radiation BC and the requirement for boundedness of the solutions yield $C_2' = C_3' = 0$.

Using interfacial continuity of pressure and velocity, we obtain

$$\hat{\tilde{\phi}}_s(z,\lambda,f) = C_4' e^{\sqrt{\lambda^2-k_s^2}z} = \frac{1}{\rho_a\sqrt{\lambda^2 - k_s^2} + \rho_s j\sqrt{k_a^2 - \lambda^2}}\left(\frac{-1}{\mu_a + j\sqrt{k_a^2 - \lambda^2}}\right)\frac{\beta_a\mu_a}{\rho_a C_p} e^{\sqrt{\lambda^2-k_s^2}z}\hat{\tilde{I}}(f,\lambda). \quad (16)$$

Range III: $k_s < k_a < \lambda$. The solutions are

$$\hat{\tilde{\phi}}_a(z,\lambda,f) = C_1'' e^{-\sqrt{\lambda^2-k_a^2}z} + C_2'' e^{\sqrt{\lambda^2-k_a^2}z} + C_s\hat{\tilde{I}}(f,\lambda)e^{-\mu_a z}, \quad (17a)$$

$$\hat{\tilde{\phi}}_a(z,\lambda,f) = C_1'' e^{-\sqrt{\lambda^2-k_a^2}z} + C_2'' e^{\sqrt{\lambda^2-k_a^2}z} + C_s\hat{\tilde{I}}(f,\lambda)e^{\mu_a z}. \quad (17b)$$

Boundedness requires $C_2'' = C_3'' = 0$.

The conditions of pressure and velocity continuity at the interface yield

$$\hat{\tilde{\phi}}_s(z,\lambda,f) = C_4'' e^{\sqrt{\lambda^2-k_s^2}z} = \frac{-\left(\mu_a - \sqrt{\lambda^2 - k_a^2}\right)}{\sqrt{\lambda^2 - k_s^2} + \frac{\rho_s}{\rho_a}\sqrt{\lambda^2 - k_a^2}}\left(\frac{1}{\mu_a^2 + k_a^2 - \lambda^2}\right)\frac{\beta_a\mu_a}{\rho_a C_p} e^{\sqrt{\lambda^2-k_s^2}z}\hat{\tilde{I}}(f,\lambda). \quad (18)$$

Now taking the piecewise inverse Hankel transform of Eqs. (14), (16), and (18), gives

$$\tilde{\phi}_s(z,r,f) = \frac{\beta_a\mu_a}{C_p}\left\{\begin{aligned} &\int_0^{k_s}\frac{je^{j\sqrt{k_s^2-\lambda^2}z}\hat{\tilde{I}}(f,\lambda)}{\left(\mu_a + j\sqrt{k_a^2-\lambda^2}\right)\left(\rho_s\sqrt{k_a^2-\lambda^2} + \rho_a\sqrt{k_s^2-\lambda^2}\right)}\lambda J_0(\lambda r)d\lambda \\ &+ \int_{k_s}^{k_a}\frac{-e^{\sqrt{\lambda^2-k_s^2}z}\hat{\tilde{I}}(f,\lambda)}{\left(\mu_a + j\sqrt{k_a^2-\lambda^2}\right)\left(\rho_a\sqrt{\lambda^2-k_s^2} + \rho_s j\sqrt{k_a^2-k_r^2}\right)}k_r J_0(\lambda r)d\lambda \\ &+ \int_{k_a}^{+\infty}\frac{-e^{\sqrt{\lambda^2-k_s^2}z}\hat{\tilde{I}}(f,\lambda)}{\left(\mu_a + \sqrt{\lambda^2-k_a^2}\right)\left(\rho_a\sqrt{\lambda^2-k_s^2} + \rho_s\sqrt{\lambda^2-k_a^2}\right)}k_r J_0(\lambda r)d\lambda \end{aligned}\right\}. \quad (19)$$

Redistribution subject to ASA license or copyright; see http://acousticalsociety.org/content/terms. Download to IP: 128.100.49.199 On: Thu, 24 Mar 2016 21:40:34

The transform of the pressure at the transducer location is

$$\tilde{p}_s(z=-L,r=0,f) = -j\omega\rho_s\tilde{\phi}(z=-L,r=0,f) \quad (20)$$

C. Asymptotic solution for large laser beams

When the laser beam spot size, W, increases due to scattering inside a turbid medium or is deliberately expanded and the low frequencies become insignificant, the asymptotic solution of Eq. (20) in the limit $W \to \infty$, is expected to approach the 1D solution, Eq. (7). The minor contribution of the low frequencies can occur particularly in the FD method by specifying the lower limit of the sweep frequency range or when the low frequencies are eliminated through the transducer bandwidth acting as a band-pass filter. Here, we will show that these two conditions can be incorporated into one. Assuming a Gaussian profile for the laser beam intensity and substituting its Hankel transform into Eq. (19), yields

$$\tilde{\phi}_s(z,r=0,f) = \frac{\beta_a\mu_a}{C_p}\int_0^{+\infty} f(\lambda,k_s,k_a)\left(\lambda W^2 e^{-\lambda^2W^2/2}\right)d\lambda. \quad (21)$$

The integrand is the product of two functions. The function f, is regular (i.e., not singular) for all values of λ, since $k_s \neq k_a$ is assumed for the integrand. The function inside the parentheses approaches zero rapidly for large values of λW. For example, for $C=\lambda W=4$, we obtain $\lambda W^2 e^{-\lambda^2W^2/2} = 1.34\times 10^{-3}W$. The integration can be cut off for $\lambda > C/W$. Furthermore, assuming $k_s, k_a \gg C/W$, the denominators simplify: $\sqrt{k_s^2-\lambda^2} \sim k_s$, $\sqrt{k_a^2-\lambda^2} \sim k_a$. It can be seen that by increasing W, the required lower frequency 1-D threshold decreases. Equation (21) becomes

$$\tilde{\phi}_s(z,r=0,f) \approx \frac{\beta_a\mu_a}{C_p}\left(\frac{j}{\mu_a+jk_a}\right)\left(\frac{1}{\rho_s k_a+\rho_a k_s}\right) \times \tilde{I}(f)e^{jk_s z}\int_0^{C/W}\lambda W^2 e^{-\lambda^2W^2/2}d\lambda. \quad (22)$$

Since $\int_0^{C/W}\lambda W^2 e^{-\lambda^2W^2/2}d\lambda \approx 1$, $\tilde{\phi}_s(z,r=0,f)$ simplifies further and the transform of the pressure field, Eq. (20), becomes

$$\tilde{p}_s(z,r=0,f) \approx -j\omega\rho_s\frac{\beta_a\mu_a}{C_p}\left(\frac{j}{\mu_a+jk_a}\right)\left(\frac{1}{\rho_s k_a+\rho_a k_s}\right) \times \tilde{I}(\omega)e^{jk_s z}, \quad (23)$$

which is Eq. (7), the 1D solution at $z=-L$. Assuming the increased diameter of the laser spot, W, due to scattering at the inclusion is 6 mm and the speed of sound in the medium is 1500 m/s, setting $C=4$, and $k_a \gg C/W$ leads to $f \gg 160$ kHz. This is the frequency threshold above which the PA behavior converges to the 1D limit.

The spectra of the PA effect $[\tilde{p}(f)/\tilde{I}(f)]$ for 1D and axisymmetric solutions, Eqs. (7) and (20) excluding the delay-time term, are shown in Fig. 2. The plots are generated for typical values of the parameters; $\mu_a = 1\,\text{cm}^{-1}$, $c_s = 1.448\,\text{mm}/\mu\text{s}$, $c_a = 1.4\,\text{mm}/\mu\text{s}$, $L=2$ cm and $W=6$ mm. It can be seen that above ~300 kHz the axisymmetric 2D spectrum approaches the 1D limit.

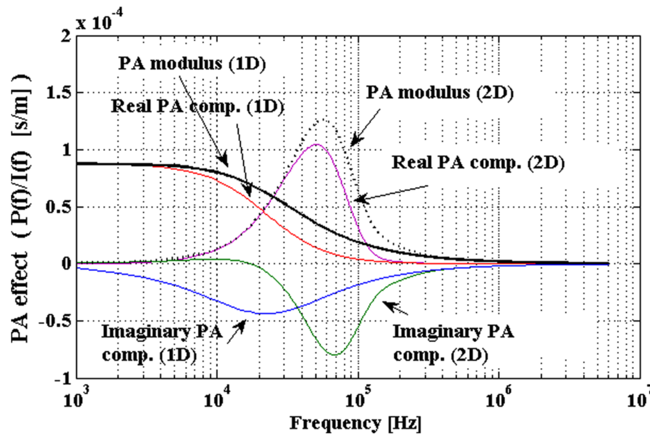

FIG. 2. (Color online) Simulated PA spectra:1D versus axisymmetric solution. (Typical values of parameters are used; $\mu_a = 1\,\text{cm}^{-1}, c_s = 1448\,\text{m/s}, c_a = 1400\,\text{m/s}, L = 2\,\text{cm}, W = 6\,\text{mm}$)

D. Acoustic attenuation effect

The effect of acoustic attenuation can be added to the model by substituting the complex wave number in the scattering medium, which modifies the 1D Eq. (7) as follows:

$$\tilde{p}_s(-L,f) = \frac{\Gamma_a e^{-\mu_{\text{eff}}L}}{\left(1+\frac{\rho_a c_a}{\rho_s c_s}\right)}\frac{\mu_a}{\mu_a c_a + j\omega}e^{-j(\omega/c_s)L}e^{-\alpha_s' L}\tilde{I}_0(f), \quad (24)$$

where α_s' is the acoustic attenuation coefficient in Np/cm. This coefficient is frequency dependent. For human breast tissue: $\alpha_s' = \alpha_s f$; $\alpha_s = 0.75\text{dB/MHz}\times\text{cm}$,[32] where the coefficient α_s is reported in the 1 to 10 MHz range (at 37 °C), however, it also makes a good approximation at frequencies below 1 MHz, although the effect is negligible at low frequencies.

E. Ultrasonic transducer model

The transfer function of the transducer is a crucial piece of information in understanding the PA response and can be added to the PA system model using the well-known Krimholtz–Leedom–Matthaei model (KLM)[36] [Fig. 3(a)]. Geometric parameters, as well as focal distances, resonance frequencies, and Q-factors can be obtained from manufacturer-provided information. Here, we used the transducer model as a transmitter, which is broadly available in the literature.[37] Using the reciprocity property of piezomaterials, the model can be applied for a receiver transducer with a scaling factor.[38] The ratio of transmitted pressure to the input voltage in transmission mode is derived using the KLM model[39]

$$\frac{\tilde{p}_t(f)}{\tilde{V}_t(f)} = \frac{\phi Z_M}{Z_{\text{in\_KLM}}}\left(\frac{e^{jkd/2}-\Gamma_B e^{-jkd/2}}{e^{jkd}-\Gamma_M\Gamma_B e^{-jkd}}\right)(1+\Gamma_M), \quad (25)$$

Redistribution subject to ASA license or copyright; see http://acousticalsociety.org/content/terms. Download to IP: 128.100.49.199 On: Thu, 24 Mar 2016 21:40:34

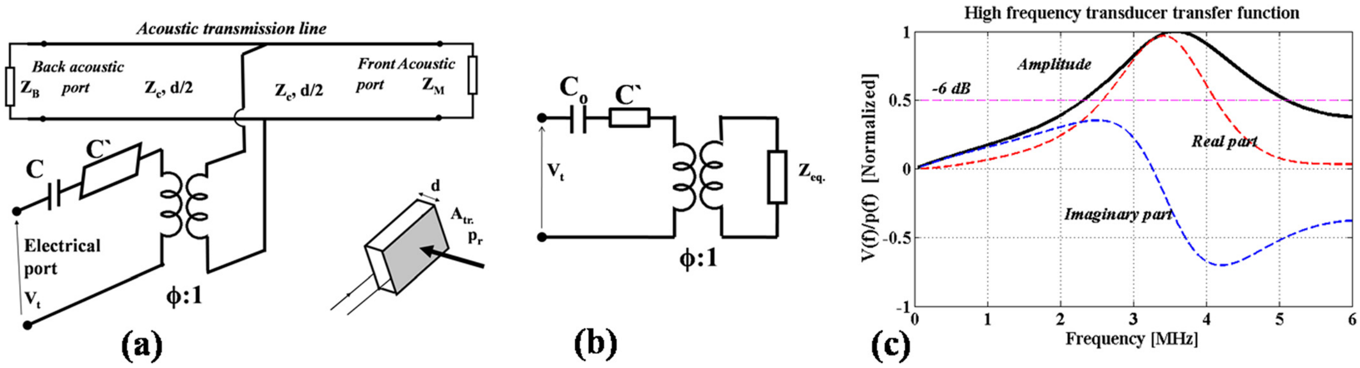

FIG. 3. (Color online) (a) KLM model transmission-line of piezoelectric transducer (Ref. 37). (b) Simplified electrical model. Z_c, Z_B, Z_M are the acoustic impedances of piezoelectric element, backing, and matching layers, respectively; d is the thickness of the piezoelectric element; V_t is the voltage at the electrical port of the transducer, p_r is the received pressure on the surface of the transducer; A_{tr} is the area of the transducer; C_0 is the electric capacitances of the transducer; C' is an equivalent capacitance defined in Eq. (28b); and ϕ is the turns ratio. (c) Transfer function of the high-frequency transducers.

where Z_s, Z_M, Z_B, Z_c are the specific acoustic impedances of the surrounding medium, matching layer, backing layer, and piezoelement, respectively. d is the piezoelement thickness and

$$\Gamma_M = \frac{Z_s - Z_M}{Z_s + Z_M}, \quad \Gamma_B = \frac{Z_s - Z_B}{Z_s + Z_B}. \tag{26}$$

$Z_{\mathrm{in\_KLM}}$ is the transducer impedance when looking into the electrical port [Fig. 3(b)], and defined by[40]

$$Z_{\mathrm{in\_KLM}} = \frac{1}{j2\pi f C_0} + \frac{1}{j2\pi f C'} + \phi^2 Z_{\mathrm{eq}}, \tag{27}$$

where ϕ (turns ratio) and C' are as follows:

$$\phi = k^t \sqrt{\frac{\pi}{\omega_0 C_0 Z_c}} \frac{\sin(\pi f/2f_0)}{\pi f/2f_0}, \tag{28a}$$

$$C' = \frac{-C_0}{(k^t)^2} \frac{(\pi f/f_0)}{\sin(\pi f/f_0)}, \tag{28b}$$

where f_0 and ω_0 are the resonance frequency and angular frequency of the transducer. k^t is the effective piezoelectric coupling coefficient. C_0 is the electric capacitance of the transducer and can be calculated by determining the piezoceramic thickness corresponding to the half wavelength of the resonance frequency and the area of the transducer. However, a more accurate method for estimating the clamped capacitance is to measure the unclamped electric capacitance with an ordinary multi-meter, and utilize the permittivity of the clamped and unclamped piezomaterial.[32] The second method is more reliable as the effective area of the transducer is not necessarily the geometric area. The measured unclamped capacitances are 850 and 1180 pF and the corresponding estimated clamped capacitances are 462 and 642 pF for our 3.5 MHz and 500 kHz transducers, respectively. Z_{eq} in Eq. (27) is the acoustic impedance of the transducer replaced in the electrical circuit [Fig. 3(b)] and can be calculated as

$$Z_{\mathrm{eq}} = \frac{Z_c\left[Z_M + jZ_c \tan\left(\frac{f\pi}{2f_0}\right)\right]\left[Z_B + jZ_c \tan\left(\frac{f\pi}{2f_0}\right)\right]}{\left[Z_M + jZ_c \tan\left(\frac{f\pi}{2f_0}\right)\right]\left[Z_c + jZ_M \tan\left(\frac{f\pi}{2f_0}\right)\right] + \left[Z_B + jZ_c \tan\left(\frac{f\pi}{2f_0}\right)\right]\left[Z_c + jZ_B \tan\left(\frac{f\pi}{2f_0}\right)\right]}. \tag{29}$$

The normalized transfer function [Eq. (25)] of the high-frequency transducer is plotted in Fig. 3(c). To employ this model for a receiver transducer, a scaling factor must be used, otherwise, the sensitivity (η) can be measured at the center frequency and, in combination with the normalized transfer function, the complete role of the transducer can be quantified in pulsed and FD PA signal detection. Using a calibrated hydrophone, the sensitivity of the 3.5 MHz transducer was measured and was shown that it operates at 31.8 μV/Pa at the center frequency.

F. PA signal and SNR

Using the PA formulation and transducer transfer function model, the detected PA response voltage is

$$V_{\mathrm{tr}}(t) = \mathcal{F}^{-1}\{\tilde{P}(f) \cdot \eta \tilde{H}_{\mathrm{tr}}(f)\}. \tag{30}$$

The above formula can be used for both pulsed and FD modes. In the FD method, the acoustic delay time can be found by determining the cross correlation, $R(t)$, of output and input signals.

$$R(t) = \mathcal{F}^{-1}\{V_{\mathrm{tr}}(f) \cdot \tilde{I}_0^*(f)\}. \tag{31}$$

The input signal is the intensity of the laser beam (W/cm^2). For a linear frequency modulation (LFM) waveform, $I_0(t)$ becomes

$$I_0(t) = A_I\left[1 + \cos\left(\omega_c t + \frac{\pi B_{\mathrm{ch}}}{T_{\mathrm{ch}}} t^2\right)\right], \quad -\frac{T_{\mathrm{ch}}}{2} < t < \frac{T_{\mathrm{ch}}}{2}, \tag{32}$$

Redistribution subject to ASA license or copyright; see http://acousticalsociety.org/content/terms. Download to IP: 128.100.49.199 On: Thu, 24 Mar 2016 21:40:34

where A_I is the average power measured by a power meter. T_{ch} and B_{ch} are the duration and frequency bandwidth of the chirp, respectively, and ω_c is the center angular frequency of the chirp. In the cross correlation process, the detected signal is multiplied by the complex conjugate of the input signal. The dc part of the input signal is eliminated and the amplitude of the waveform is normalized to produce the reference signal, $\tilde{I}^*_{\mathrm{ref}}(f)$. Using the 1D model, Eq. (24), $R(t)$ is written as

$$R(t) = \left(\frac{\Gamma_a e^{-\mu_{\mathrm{eff}}L}}{1+\frac{\rho_a c_a}{\rho_s c_s}}\right)\mathcal{F}^{-1}\left\{\left(\frac{\mu_a}{\mu_a c_a + j\omega}\right)e^{-j(\omega/c_s)L}e^{-\alpha_s f L}\eta H_{\mathrm{tr}}(f)\tilde{I}_0(f)\cdot\tilde{I}^*_{\mathrm{ref}}(f)\right\}. \tag{33}$$

The procedure for axisymmetric solution is similar. To estimate the detected signal, the fact that the peak value of the cross correlation is the total spectral energy of the matched filter output must be taken into account:

$$R_{\max}\left(t=\frac{L}{c_s}\right) = \left(\frac{\Gamma_a e^{-\mu_{\mathrm{eff}}L}}{1+\frac{\rho_a c_a}{\rho_s c_s}}\right)\int_{-\infty}^{+\infty}\left(\frac{\mu_a}{\mu_a c_a + j\omega}\right)e^{-\alpha_s f L}\eta\tilde{H}_{\mathrm{tr}}(f)\tilde{I}_0(f)\cdot\tilde{I}^*_{\mathrm{ref}}(f)df. \tag{34}$$

For the chirp bandwidth we can substitute the rectangular bandwidth approximation $\tilde{I}_0(f)\cdot\tilde{I}^*_{\mathrm{ref}}(f)\simeq A_I(T_{ch}/4B_{ch})$.[35] A combination of the in-phase and the quadrature signals yields

$$R_{\max}\approx\left(\frac{2\Gamma_a\mu_a e^{-\mu_{\mathrm{eff}}L}\eta}{1+\frac{\rho_a c_a}{\rho_s c_s}}\right)\left(A_I\frac{T_{ch}}{4B_{ch}}\right)\times\left[\int_{f_c-B_{ch}/2}^{f_c+B_{ch}/2}\left(\frac{e^{-\alpha_s f L}}{\mu_a c_a + j\omega}\right)\tilde{H}_{\mathrm{tr}}(f)df\right]_{\max}, \tag{35}$$

where "max" on the right-hand-side refers to the maximum of real and imaginary values. These two maxima are not at the same delay time, however, the quadrature maximum is also located inside the axial resolution limit (full width at half maximum) of the envelope signal. It should be considered that through the cross correlation algorithm, the noise is also multiplied by a factor $\sqrt{T_{ch}/4B_{ch}}$ through the complex conjugate of the reference signal. The phase change induced in noise is ignored as it does not affect the noise level. Therefore, to find the optimal bandwidth which maximizes the cross correlation signal, the ratio

$$\frac{R_{\max}}{\sqrt{\frac{T_{ch}}{4B_{ch}}}} = \left(\frac{\Gamma_a\mu_a e^{-\mu_{\mathrm{eff}}L}\eta A_I}{1+\frac{\rho_a c_a}{\rho_s c_s}}\right)\sqrt{\frac{T_{ch}}{B_{ch}}}\left|\int_{f_c-B_{ch}/2}^{f_c+B_{ch}/2}\left(\frac{e^{-\alpha_s f L}}{\mu_a c_a + j\omega}\right)\times\tilde{H}_{\mathrm{tr}}(f)df\right|_{\max} \tag{36}$$

must be maximized. The SNR of the cross correlation signal[41] is given by

$$\mathrm{SNR_{CW}} = \frac{|R(t)|^2_{\max}}{N_{\mathrm{out}}} = \frac{\left(\frac{2\Gamma_a\mu_a e^{-\mu_{\mathrm{eff}}L}\eta A_I}{1+\frac{\rho_a c_a}{\rho_s c_s}}\frac{T_{ch}}{4B_{ch}}\right)^2\left|\int_{f_c-B_{ch}/2}^{f_c+B_{ch}/2}\left(\frac{e^{-\alpha_s f L}}{\mu_a c_a + j\omega}\right)\tilde{H}_{\mathrm{tr}}(f)df\right|^2_{\max}}{N_o\int_{f_c-B_{ch}/2}^{f_c+B_{ch}/2}\left|\sqrt{\frac{T_{ch}}{4B_{ch}}}\right|^2 df}, \tag{37}$$

where N_{out} is the mean noise power of the detected signal and any noise outside the chirp bandwidth is assumed to be automatically eliminated through matched filtering. The result is

$$\mathrm{SNR_{CW}} = \frac{(\Gamma_a\mu_a e^{-\mu_{\mathrm{eff}}L}\eta A_I)^2 T_{ch}\left|\int_{f_c-B_{ch}/2}^{f_c+B_{ch}/2}\frac{e^{-\alpha_s f L}}{\mu_a c_a + j\omega}\tilde{H}_{\mathrm{tr}}(f)df\right|^2_{\max}}{\left(1+\frac{\rho_a c_a}{\rho_s c_s}\right)^2 N_{\mathrm{out}}B^2_{ch}}. \tag{38}$$

Equation (38) is very useful for comparing the SNR of the FD-PA with the pulsed laser PA. This equation shows that SNR is proportional to the chirp duration. It is also known that SNR is proportional to the number of averages in the case of repetitive excitation.[35] Therefore, T_{ch} in Eq. (38) can be considered as the total exposure duration.

III. EXPERIMENTAL RESULTS AND THEORETICAL SIMULATIONS

Theoretical simulations were performed for both pulsed transient and cross correlation signals and were compared with experimental results. The experiments were

Redistribution subject to ASA license or copyright; see http://acousticalsociety.org/content/terms. Download to IP: 128.100.49.199 On: Thu, 24 Mar 2016 21:40:34

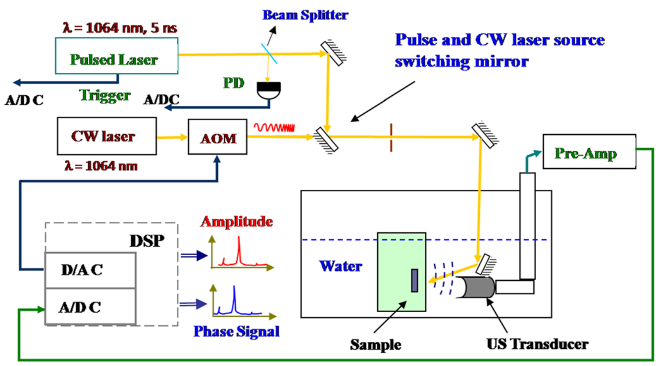

FIG. 4. (Color online) Block diagram of the experimental setup. The laser source can be switched between pulsed and CW lasers with sliding one mirror.

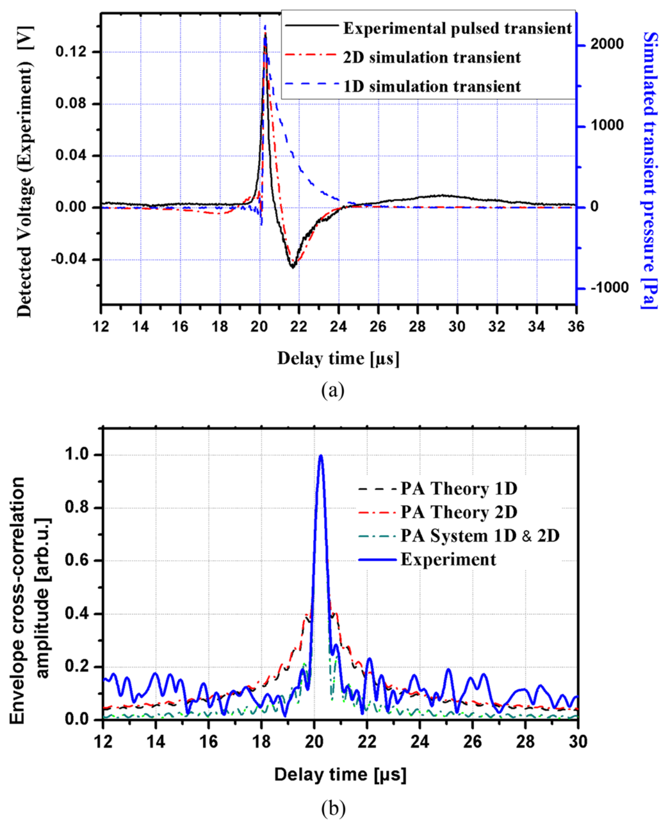

FIG. 5. (Color online) (a) Experimental pulsed transient versus 1D and axisymmetric pressure transients. Best-fit parameters: $\mu_a = 4\,\mathrm{cm}^{-1}$, $c_s = 1440\,\mathrm{m/s}$, $c_a = 1400\,\mathrm{m/s}$, $L = 1\,\mathrm{cm}$, $\mu_{\mathrm{eff}} = 1.3\,\mathrm{cm}^{-1}$. (b) Experimental cross correlation signal versus simulations of the cross correlation of the pressure waveform and detected voltage signal. The "PA system" accounts for transducer contribution as well as PA effect and 1D and 2D simulations coincide.

performed using our dual-mode PA system,[25] where pulsed and CW lasers were employed on the same sample (Fig. 4). The wavelength of both lasers was 1064 nm. The CW source features a fiber laser (IPG Photonics, Boston, MA) and an acousto-optic modulator which modulates the laser intensity according to waveforms defined in the software function generator. The pulsed source was a Q-switched Nd:YAG laser (Continuum, Santa-Clara, CA) which produces pulses of 5.2 ns duration. Two single focused ultrasonic transducers were used with central frequencies 0.5 and 3.5 MHz, bandwidths 0.32 to 0.63 MHz and 2.66 to 5.23 MHz, and focal lengths 5.27 and 2.54 cm, respectively. The function generation, signal acquisition, and processing were implemented using the LABVIEW platform (National Instruments, Austin, TX).

The sample was a thick plastisol material with absorption coefficient 4 cm^{-1}, located at a depth of 10 mm in 47% Intralipid solution. The energy fluence of the irradiated pulsed laser was 100 $\mathrm{mJ/cm}^2$, and the utilized intensity of the CW laser was 15.6 $\mathrm{W/cm}^2$ (250 ms laser exposure time).

The experimental pulsed transient and corresponding 1D and 2D axisymmetric simulated pressure transients are shown in Fig. 5(a). The laser fluence on the absorber was calculated for both cases using exponential attenuation and spherical propagation [Eq. (8)] to attain consistent results. Equations (7) and (20) were solved where the irradiation (I_0) is considered a very short rectangular pulse. For the 2D solution a Gaussian radial profile was assumed for the laser beam. The simulated pressure transients show approximately similar peak values for 1D and 2D solutions, however, the 1D solution is not capable of predicting the bipolar shape of the signal and the peak width, whereas the 2D solution can be used to predict such details.

The FD envelope signal trace obtained by utilizing a LFM chirp with frequency sweep 200 kHz to 3 MHz was compared with simulations in Fig. 5(b). The results of the 1D and 2D solutions are very close [Eqs. (7) and (20)] and coincided completely when the transducer effect was considered. The cross correlation signal incorporating the effect of the transducer ["PA system" in Fig. 5(b)] shows that the transducer transfer function acts as a window reducing the sidelobes. This conclusion is consistent with previous experimental results.[29]

IV. PHOTOACOUSTIC RADAR PARAMETER OPTIMIZATION

A. Optimal chirp bandwidth

In this section we present experiments and theoretical procedures carried out to determine the optimal bandwidth of the LFM chirp for different ultrasonic transducers. It was shown in our earlier measurements[29] that for a high frequency transducer (center frequency 3.5 MHz), the largest available frequency range is not optimal, and the optimal bandwidth may not be symmetric around the center frequency. In those experiments, we showed that among three bandwidths; 0.5–3 MHz, 1–3 MHz, and 0.5–5 MHz, the first frequency range generates the highest SNR. In this work, the lower bandwidth limit for the same sample was reduced. The sample used in this experiment was a flat plastisol inclusion 6 mm beneath plastisol surroundings. The absorption coefficients of inclusion and surroundings were 4 and 0.2 cm^{-1}, respectively, and the reduced scattering coefficient of the surroundings was 3.1 cm^{-1}. The signal traces generated with several bandwidths are shown in Fig. 6. In the signal traces, two peaks are visible which correspond to the surface of the plastisol (at $\sim$17 μs) and to the inclusion (at $\sim$21 μs). The SNRs shown in the inset were calculated according to the definition in Eq. (37) based on the later peaks due to the inclusion. It can be seen that the optimal bandwidth is 200 kHz to 3 MHz, which is far below

Redistribution subject to ASA license or copyright; see http://acousticalsociety.org/content/terms. Download to IP: 128.100.49.199 On: Thu, 24 Mar 2016 21:40:34

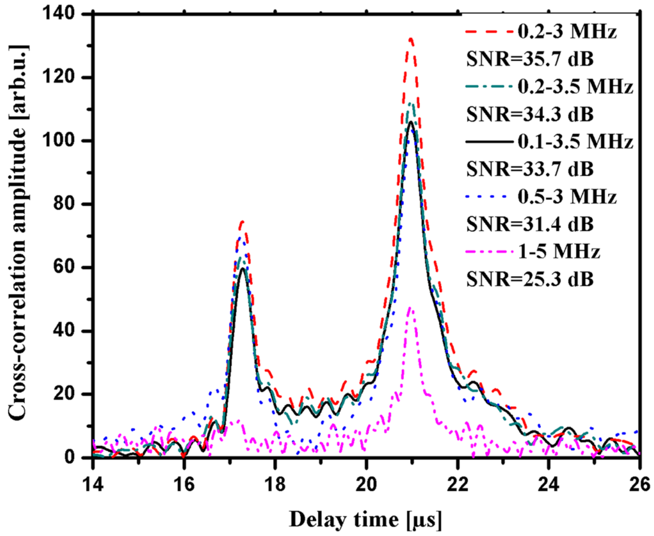

FIG. 6. (Color online) Experimental PA bandwidth optimization of the frequency modulation chirp with a 3.5 MHz transducer. The sample consisted of an absorber with 4 cm^{-1} absorption coefficient, 6 mm beneath the surface of plastisol with reduced scattering and absorption coefficients of 3.1 and 0.2 cm^{-1}, respectively. The laser spot size on the plastisol surface was 2 mm.

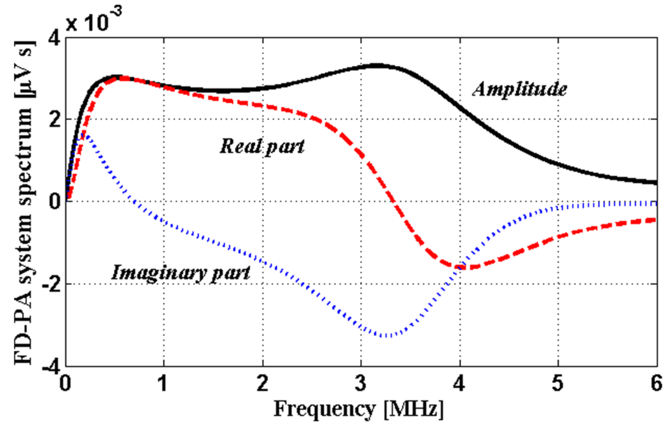

FIG. 7. (Color online) PA system frequency response, consisting of the PA response, the acoustic attenuation and the high-frequency transducer transfer function. Typical parameters used: $\mu_a = 4\,\mathrm{cm}^{-1}$, $c_s = 140\,\mathrm{m/s}$, $\alpha_s = 0.0863\,\mathrm{Np/cm}$ (human breast), $L = 2$ cm.

the range of the transducer. This bandwidth enhanced the SNR by 10 dB over the largest bandwidth, 1 to 5 MHz.

A similar experiment was conducted with the low frequency transducer. The tested sample had similar physical properties to the one described above, only the inclusion was located approximately 14 mm below the surface. Several bandwidths were tested with 200 kHz used as the low cutoff frequency of the chirp. The upper cutoff frequencies were set to 700, 800, 850, and 900 kHz, and the corresponding measured SNRs were 17.5, 17.8, 18.1, and 17.7 dB, respectively. This experiment showed that the optimal bandwidth is 200 to 850 kHz, however, the SNR variation was very small, with a maximum of 0.6 dB.

The theory developed in Sec. II can be used to interpret the experimental results. The cross correlation signal is affected by three factors: The physics of the PA response, the acoustic attenuation of the propagating waves in the medium and the transducer transfer function [Eq. (35)]. The frequency dependence (spectrum) of the integrand of Eq. (36) for the high-frequency transducer with typical parameters is shown in Fig. 7. This figure shows that the rising part of the transducer transfer function amplitude compensates for the PA response decay and the acoustic attenuation and is followed by a rapid decrease above this frequency region. This spectrum explains why a frequency range below the center frequency generates the optimal bandwidth for a high frequency transducer. Equation (36) can be used to determine the bandwidth which generates the highest peak signal. With a high-frequency transducer, when the lower frequency was decreased from 500 to 200 kHz, the SNR increased, however, decreasing the lower frequency to 100 kHz did not augment the SNR. The lower limit of the bandwidth was fixed at 200 kHz, and the maximum signal was calculated, depending on the variation of the upper limit of the bandwidth for both transducers. The most important physical property involved here is the value of the optical absorption coefficient. The variation of speed of sound in tissue is less than 10%.[1] Therefore the calculations were performed for absorption coefficients between 0.2 and 10 cm^{-1}. The other parameters used in Figs. 7 and 8 are typical values for soft tissues. The chromophore was assumed to be 2-cm deep. Plots in Fig. 8(a) show the peak variation for the high-frequency transducer. The figure shows that the absorption coefficient has minor impact on the optimal bandwidth and the best upper cutoff frequency is between 2.9 to 3 MHz, which is completely consistent with the experimental results, Fig. 6. The two maximum points in Fig. 8(a) correspond to the maxima of the real and imaginary part, respectively [Eq. (36)]. We should mention that the depth of 2 cm was selected as it is around the maximum depth at which our system was able to detect absorbers with high frequency transducer. The SNR was maximized for the deepest possible absorbers to increase depth detectivity. However, variation in L in the range of 0.5 to 3 cm will generate a very small deviation in the optimal bandwidth.

Similar calculations for the low-frequency transducer are shown in Fig. 8(b). In this case the optimal maximum frequency was found to be between 700 to 800 kHz (750 kHz for $\mu_a = 4\,\mathrm{cm}^{-1}$), which is within 100 kHz of the experimental results. Figure 8(b) predicts that the variation of the cross correlation peak for an upper cutoff frequency between 700 and 900 kHz is less than 0.7 dB, as was borne out experimentally.

The reason for optimizing the bandwidth with respect to maximum matched filter signal, Eq. (36), and not the maximum SNR, Eq. (38), is that using the latter equation one finds a single spike at the location of the maximum of the spectrum (Fig. 7). This zero bandwidth result indicates that the optimization constraints are not properly set. The main constraint is the requirement for large bandwidth so as to minimize the sidelobes, which is not accounted for in Eq. (38). Our experiments demonstrate that the achieved bandwidth with Eq. (36) is very close to the one generating the highest SNR experimentally. This is consistent with the pure ultrasound case where the optimal bandwidth was determined based on the maximum cross correlation peak.[14] It

Redistribution subject to ASA license or copyright; see http://acousticalsociety.org/content/terms. Download to IP: 128.100.49.199 On: Thu, 24 Mar 2016 21:40:34

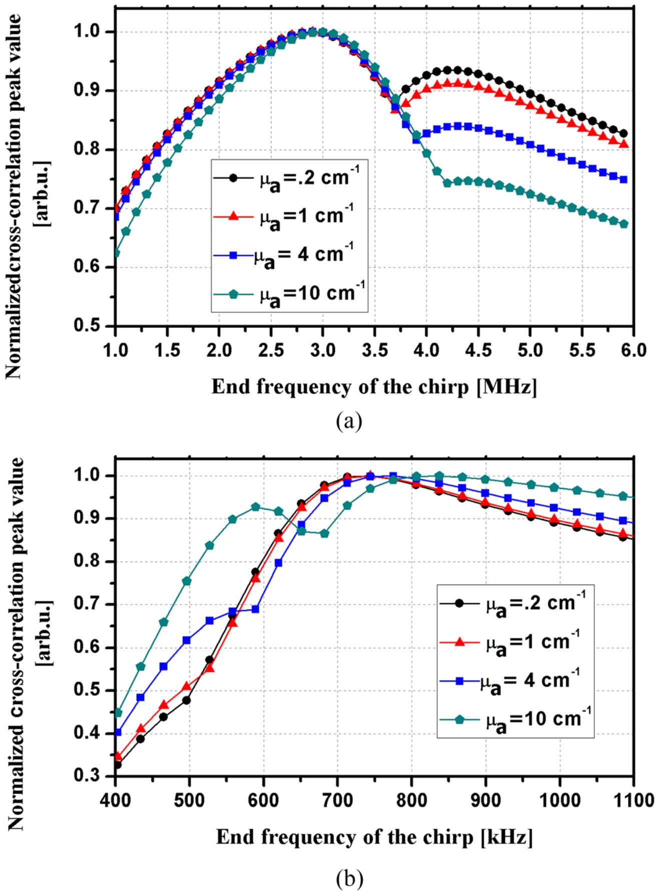

FIG. 8. (Color online) Predicted chirp optimal bandwidth that generates the highest detected cross correlation signal. (a) 3.5 MHz transducer, (b) 0.5 MHz transducer.

should be noted that while the optimal bandwidth maximizes the SNR, it may be less than the transducer bandwidth, therefore, it could compromise the axial resolution for SNR. However, it has been shown that when the SNR is low, high resolution does not help to distinguish chromophores at different depths.[35]

This procedure can also be applied to the determination of the optimal lower cutoff frequencies. These frequencies are important for deep tissue penetration and imaging. However, experiments reveal that at low frequencies, the effect of the lateral degrees-of-freedom for PA wave generation and propagation is significant and requires a more detailed investigation. This effect can generate artifacts or false peaks in the A-scans. This is discussed in the next section.

The same procedure can also be repeated using the axisymmetric PA solution. The deviation in the plots will be very small for high-frequency and visible for low-frequency bandwidths. However in both cases the deviations of the optimal bandwidths are very small. Furthermore, it should be noted that the spatial resolution of our imager cannot be better than the transducer lateral resolution (0.87 and 5.4 mm for high- and low-frequency transducers). Therefore this PA system is applicable for detection of chromophores a few millimeters in size. On the other hand, to detect smaller objects, the frequency range of the employed transducer should be higher and therefore, still consistent with the 1D approximation. Experimentally generated signals from inclusions as small as 2 mm demonstrate the applicability of the foregoing theory.[35]

B. Low-frequency effects on FD PA

The low cutoff frequency of the modulated signal can affect PA *A*-scans and images. An experiment was implemented with the low-frequency transducer and the same plastisol sample mentioned in the previous section. Using the same procedure, the lower limit of the frequency range was decreased from 200 kHz to 150 and 100 kHz. Figure 9 shows the experimental *A*-scans, where two peaks correspond to the sample surface and to a subsurface inclusion (arrow). On decreasing the low cutoff frequency, an extra peak appeared (at ~35 μs) and grew beside the first (surface) peak. One factor contributing to the generation of these large false peaks is acoustic diffraction due to the small laser spot size (~2 mm) on the plastisol surface which is commensurate with the acoustic wavelength. Using the 2D theory, the generation of the first cross correlation peak and its adjacent artifacts were simulated. Figure 10 shows the results of these simulations for a medium with an absorption coefficient 0.2 cm^{-1} when employing the aforementioned three bandwidths. Figure 10 also compares the experimental and simulated *A*-scans for a frequency sweep between 150 and 800 kHz. Only the first peak on the surface of the plastisol is simulated and demonstrates how a small laser spot size and low-frequency excitation can cooperate to produce artifacts.

In the high-frequency *A*-scans presented in Fig. 6, it can be seen that the sidelobes grow by extending the frequency range to low frequencies. However, even in the 100–3500 kHz frequency range, no extra peak artifacts appear. Although the sidelobes adjacent to the strong main peak due to the absorber which is very close to the surface peak may possibly hide such artifacts, this is not likely: The wider chirp bandwidth limits the low-frequency contribution; the higher center frequency of the transducer also diminishes the weight of low frequency contributions; and acoustic

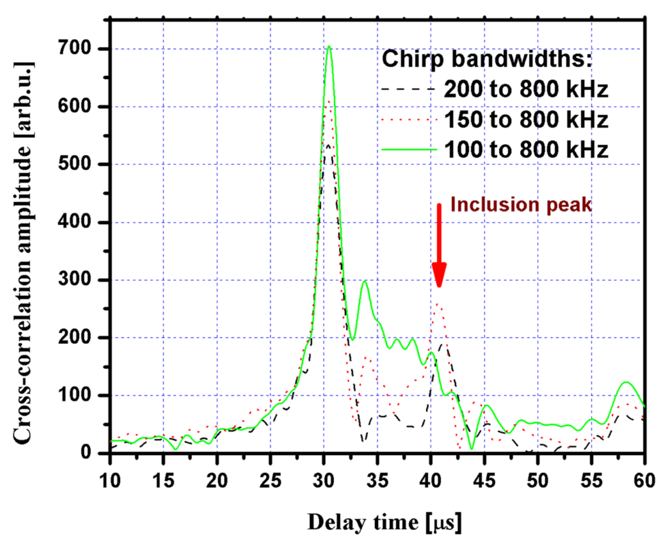

FIG. 9. (Color online) Experimental artifacts generated with the 0.5 MHz transducer in the cross correlation PA amplitude. Laser spot size: 2 mm.

Redistribution subject to ASA license or copyright; see http://acousticalsociety.org/content/terms. Download to IP: 128.100.49.199 On: Thu, 24 Mar 2016 21:40:34

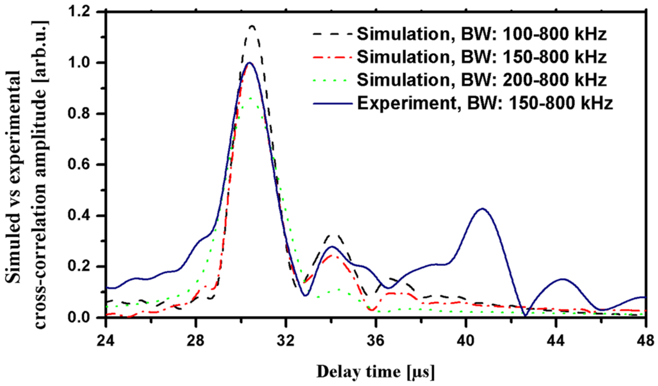

FIG. 10. (Color online) 2D simulated cross correlation signals exhibit low-frequency artifacts and comparison with experimental signal amplitude in the bandwidth 150 to 800 kHz. Laser spot size: 2 mm.

diffraction is less efficient at high frequencies at which the ultrasonic wavelength 0.94 mm is small compared to the laser beam spot size (∼2 mm).

Another experiment with the high-frequency transducer was performed in the frequency range between 200 kHz and 3 MHz. The properties of the plastisol sample were as described above. The absorbing inclusion was located ∼14 mm beneath the surface. The A-scan generated with the FD PA method is shown in Fig. 11(a). It can be seen that, although the frequency range starts at 200 kHz, there are large artifacts present in this signal trace, mostly generated by acoustic diffraction; the surface was ∼13 mm (at ∼9 μs) away from the transducer which is out of the focal zone and very close to the near field.

The low-frequency artifacts were diminished by high-pass filtering of the averaged waveform before performing the cross correlation operation. A high-pass filter able to eliminate these artifacts with a cut-off frequency of 325 kHz was employed [Fig. 11(a)]. This figure shows that by high-pass filtering, the true peaks also decrease, as they lose part of their energy content. High-pass filtering demonstrates the connection of these artifacts with low-frequencies, otherwise it is not advisable to use a bandwidth with low starting frequency and filter it afterward.

A cross-sectional image of the sample was produced from a line scan over the inclusions and as well depicted in Fig. 11(b). The surface of the plastisol and two inclusions are recognizable, although, the artifacts degrade the image. The large inclusion is a flat absorber and the small inclusion is a cylindrical absorber, 1/4 in. diameter, both with absorption coefficient 4 cm^{-1} at approximately 14 mm below the surface. Figure 11(c) also shows how the image artifacts were eliminated after high-pass filtering.

V. CONCLUSIONS

PA wave generation and propagation was modeled in axisymmetric coordinates and compared with the one dimensional solution in the frequency domain. The 1D and 2D PA spectra coincided above a few hundred kHz. It was thus concluded that a 1D PA mathematical model is sufficient for FD-PA analysis when the starting frequency is high enough. Furthermore, the 1D solution was used to relate the maximum matched filter peak and SNR to system parameters: bandwidth, chirp duration, physical properties of the sample, and transducer transfer function.

The effect of bandwidth in the generation of the FD-PA signal was investigated theoretically and experimentally. It was shown that the optimal bandwidth generating the highest SNR for a low-frequency transducer (0.5 MHz) is roughly centered at the peak frequency of the transducer. For a high-frequency transducer (3.5 MHz), however, the decaying effects of the PA response and acoustic attenuation with increasing frequency, shift the optimal bandwidth to the lower frequencies, where the rising amplitude of the transducer transfer function counterbalances those low-pass-equivalent factors. Experiments revealed that by tuning the modulated chirp bandwidth with respect to that of a high-frequency transducer, the SNR of the *A*-scan can be improved by 10 dB. It was demonstrated theoretically that by proper selection of the chirp bandwidth, the transducer can act as a window or a filter, reducing the sidelobes. As a result extra windowing was not required. This procedure amounts to frequency (spectral) fine-tuning of the PA radar.

Photoacoustic-ultrasonic diffraction effects related to laser beam spot size and ultrasonic wavelength generate artifacts at low frequencies. This effect was demonstrated experimentally and accounted for with the 2D axisymmetric

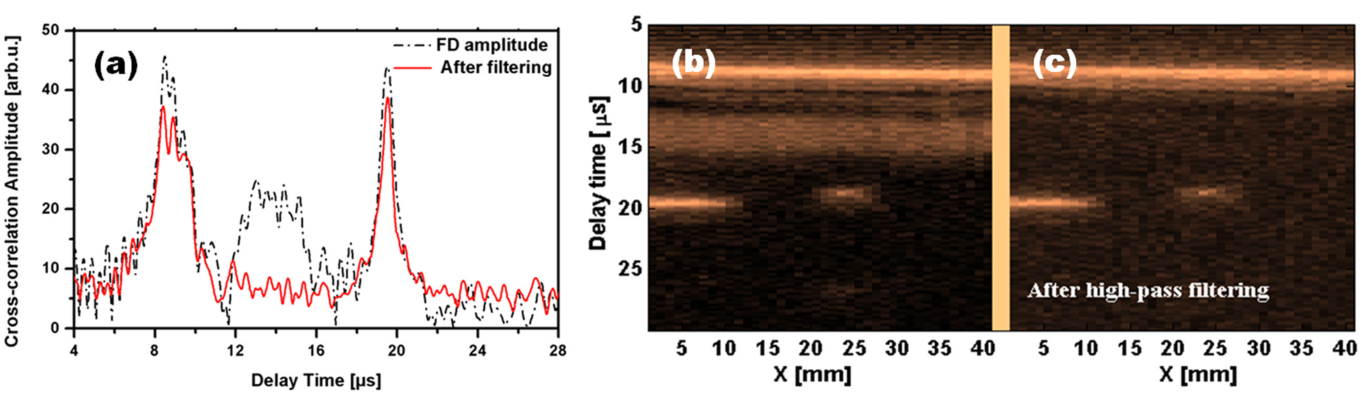

FIG. 11. (Color online) (a) A raw high-frequency *A*-scan with artifacts (frequency range: 200 kHz to 3 MHz) and the high-pass filtered cross correlation signal (laser spot size: 2 mm) and corresponding FD PA images (b) before and (c) after high-pass filtering.

Redistribution subject to ASA license or copyright; see http://acousticalsociety.org/content/terms. Download to IP: 128.100.49.199 On: Thu, 24 Mar 2016 21:40:34

theory. Thus, the starting frequency of the chirp should be selected carefully, especially when the laser spot on the surface is very small, to avoid artifacts.

ACKNOWLEDGMENTS

The authors gratefully acknowledge the support of the Canada Foundation for Innovation (CFI), the Ontario Research Fund (ORF), and the Canada Research Chairs (CRC). They further acknowledge the NSERC Strategic and Discovery Grants programs and the MRI Ontario Premier's 2007 Discovery Award in Science and Engineering to A.M.

[1]M. Xu and L.V. Wang, "Photoacoustic imaging in biomedicine," Rev. Sci. Instrum. **77**, 041101–041122 (2006).

[2]C. E. Cook and W. M. Seibert, "The early history of pulse compression radar," IEEE Trans. Aero. Elect. Syst. **24**(6), 825–833 (1988).

[3]J. H. Van Vleck and D. Middleton, "A Theoretical Comparison of the Visual, Aural, and Meter Reception of Pulsed Signals in the Presence of Noise," J. Appl. Phys. **17**, 940–971 (1946).

[4]J. R. Klauder, A. C. Price, S. Darlington, and W. J. Albersheim, "The theory and design of chirp radars," Bell Syst. Tech. J. **39**, 745–808 (1960).

[5]E. N. Fowle, D. R. Carey, R. E. Vander Schuur, and R. C. Yost, "A pulse compression system employing a linear FM Gaussian signal," Proc. IEEE **52**, 304–312 (1962).

[6]A. W. Rihaczek, "Radar waveform selection—A simplified approach," IEEE Trans. Aero. Elect. Syst. **7**(6), 1078–1086 (1971).

[7]C. E. Cook, and J. Paolillo, "A pulse compression predistortion function for efficient sidelobe reduction in a high power radar," in *Proceedings of IEEE* 52 (1964), pp. 377–389.

[8]R. E. Millett, "A matched-filter pulse-compression system using a nonlinear FM waveform," IEEE Trans. Aero. Elect. Syst. **6**(1), 73–78 (1970).

[9]Y. Takeuchi, "An investigation of a spread energy method for medical ultrasound systems—Part one: Theory and investigation," Ultrasonics **17**(4), 175–182 (1979).

[10]V. L. Newhouse, D. Cathignol, and J. Y. Chapelon, "Introduction to ultrasonic pseudo-random code systems," in *Progress in Medical Imaging*, edited by V. L. Newhouse (Springer-Verlag, New York, 1988), Chap. 5, pp. 215–226.

[11]M. O'Donnell, "Coded excitation system for improving the penetration of real-time phased-array imaging systems," IEEE Trans. Ultrason., Ferroelect., Freq. Contr. **39**, 341–351 (1992).

[12]N. A. H. K. Rao, "Investigation of a pulse compression technique for medical ultrasound: A simulation study," Med. Biol. Eng. Comp. **32**(2), 181–188 (1994).

[13]M. Pollakowski and H. Ermert, "Chirp signal matching and signal power optimization in pulse-echo mode ultrasonic nondestructive testing," IEEE Trans. Ultrason., Ferroelect., Freq. Contr. **41**, (5), 655–659 (1994).

[14]M. Pollakowski, H. Ermest, L. von Bernus, and T. Schmeidl,. "The optimum bandwidth of chirp signals in ultrasonic applications," Ultrasonics **31**(6), 416–420 (1993).

[15]T. X. Misaridis, K. Gammelmark, C. H. Jørgensen, N. Lindberg, A. H. Thomsen, M. H. Pedersen, and J. A. Jensen, "Potential of coded excitation in medical ultrasound imaging," Ultrasonics **38**, 183–189 (2000).

[16]M. H. Pedersen, T. X. Misaridis, and J. A. Jensen, "Clinical comparison of pulse and chirp excitation," in *IEEE Ultrasonics Symposium* (2002), pp. 1673–1676.

[17]T. Misaridis and J. A. Jensen, "Use of modulated excitation signals in medical ultrasound. Part I: Basic concepts and expected benefits," IEEE Trans. Ultrason., Ferroelect., Freq. Contr. **52**(2), 176–190 (2005).

[18]T. Misaridis and J. A. Jensen, "Use of modulated excitation signals in medical ultrasound, Part II: Design and performance for medical imaging applications," IEEE Trans. Ultrason., Ferroelect., Freq. Contr. **52**(**2**), 191–206 (2005).

[19]T. Misaridis and J. A. Jensen, "Use of modulated excitation signals in medical ultrasound, Part III: High frame rate imaging," IEEE Trans. Ultrason., Ferroelect., Freq. Contr. **52**(2), 207–218 (2005).

[20]Y. Fan, A. Mandelis, G. M. Spirou, and I. A. Vitkin, "Development of a laser Photothermoacoustic frequency-swept system for subsurface imaging: Theory and experiment," J. Acoust. Soc. Am. **116**(6), 3523–3533 (2004).

[21]Y. Fan, A. Mandelis, G. Spirou, I. A. Vitkin, and W. M. Whelan,. "Laser photothermoacoustic heterodyned lock-in depth profilometry of turbid tissue phantoms," Phys. Rev. E **72**, 051908–051911 (2005).

[22]S. A. Telenkov and A. Mandelis, "Fourier-domain biophotoacoustic subsurface depth selective amplitude and phase imaging of turbid phantoms and biological tissue," J. Biomed. Opt. **11**(**4**), 044006–044010 (2006).

[23]S. A. Telenkov, A. Mandelis, B. Lashkari, and M. Forcht, "Frequency-domain photothermoacoustics: Alternative imaging modality of biological tissues," J. Appl. Phys. **105**, 102029 (2009).

[24]A. Mandelis, "Bioacoustophotonic depth-selective imaging of turbid media a tissues: Instrumentation and measurements," Phys. Can. **62**, 83–90 (2006).

[25]S. A. Telenkov and A. Mandelis, "Photothermoacoustic imaging of biological tissues: maximum depth characterization comparison of time and frequency-domain easurements," J. Biomed. Opt. **14**(4), 044025 (2009).

[26]K. Maslov and L. V. Wang, "Photoacoustic imaging of biological tissue with intensity-modulated continuous-wave laser," J. Biomed. Opt. **13**(2), 024006 (2008).

[27]A. Petschke, and P. J. La Riviére, "Comparison of intensity-modulated continuous-wave lasers with a chirped modulation frequency to pulsed lasers for photoacoustic imaging applications," Biomed. Opt. Express **1**(4), 1188–1195 (2010).

[28]M. P. Mienkina, C.-S. Friedrich, N. C. Gerhardt, W. G. Wilkening, M. R. Hofmann, and G. Schmitz, "Experimental Evaluation of Photoacoustic Coded Excitation Using Unipolar Golay Codes," *IEEE Trans. Ultrason., Ferroelect., Freq. Contr*. **57**(7), 1583–1593 (2010).

[29]B. Lashkari and A. Mandelis, "Photoacoustic radar imaging; signal-to-noise ratio, contrast, and resolution enhancement using nonlinear chirp modulation," Opt. Lett. **35**(10), 1623–1625 (2010).

[30]G. J. Diebold and T. Sun, "Properties of optoacoustic waves in one, two, and three dimensions," Acustica **80**, 339–351 (1994).

[31]V. E. Gusev and A. A. Karabutov, *Laser Optoacoustics* (American Institute of Physics, New York, 1993), Chap. 2.

[32]R. S. C. Cobbold, *Foundations of Biomedical Ultrasound* (Oxford University Press, New York, 2007), pp. 76, 87, and 346.

[33]A. Mandelis, N. Baddour, Y. Cai, and R. G. Walmsley, "Laser-induced photothermoacoustic pressure-wave pulses in a polystyrene well and water system used for photomechanical drug delivery," J. Opt. Soc. Am. B **22**(5), 1024–1036 (2005).

[34]A. Mandelis and C. Feng, "Frequency-domain theory of laser infrared photothermal radiometric detection of thermal waves generated by diffuse-photon-density wave fields in turbid media," Phys. Rev. E **65**, 021909–021919 (2002).

[35]B. Lashkari, Ph.D. thesis, Mechanical and Industrial Engineering, University of Toronto, 2011, Chaps. 3 and 5.

[36]D. Leedom, G. Matthaei, and R. Krimholtz, "New Equivalent Circuits for Elementary Piezoelectric Transducers," Electron. Lett. **6**, 398–399 (1970).

[37]G. S. Kino, *Acoustic Waves: Devices, Imaging, and Analog Signal Processing* (Prentice-Hall, Englewood Cliffs, NJ, 1987), pp. 41–71.

[38]T. L. Rhyne, "Characterizing ultrasonic transducers using radiation efficiency and reception noise figure," IEEE Trans. Ultrason., Ferroelect., Freq. Contr. **45**, 559–566 (1998).

[39]T. A. Bigelow, "Experimental evaluation of nonlinear indices for ultrasound transducer characterizations," M.Sc. thesis, University of Illinois at Urbana–Champaign, 2001, Appendix B.

[40]C. S. Desilets, J. D. Fraser, and G. S. Kino, "The design of efficient broad-band piezoelectric transducers," IEEE Trans. Sonics Ultrasonics, **SU-25**(3), 115–125 (1978).

[41]M. Skolnik, *Introduction to Radar Systems* (McGraw-Hill, New York, 1962), p. 411.

Redistribution subject to ASA license or copyright; see http://acousticalsociety.org/content/terms. Download to IP: 128.100.49.199 On: Thu, 24 Mar 2016 21:40:34